Chapter 3

Jet Kinematics

3.1 Introduction

Combining the data described in Chapter 2 with the older observations listed in Appendix A, we can determine and analyze apparent and real motions of the jet components in 3C345. The apparent velocity and apparent distance traveled along the jet are model independent quantities, and can be measured directly. The rest of the kinematic parameters require certain prior assumptions to be made about the jet geometry. In general, the jet geometry can be described by the time variations of the jet's proper velocity. For the jet components, this implies the knowledge of the instantaneous component speed β and angle θ between the velocity vector and the line of sight. We assume that β and θ can vary simultaneously. Of these joint variations, we will describe two extreme cases: A) jet with constant viewing angle ($\beta = \beta(t), \theta = const$), and B) bent jet with constant speed ($\beta = const, \theta = \theta(t)$). We deliberatley avoid using more specific models of the jet geometry (such as the helical jet model), to minimize the number of free parameters included in the consideration. Based on the analysis of the two extreme cases, we will show that neither of them is likely to occur, and that changes of the component rest frame speeds are required for explaining the observed kinematic properties of the jet.

The "standard" cosmological model (see Weinberg 1972) with Hubble constant and deceleration parameter of $H_0 = 100h$ km s^{-1} Mpc^{-1}, $q_0 = 0.5$ was adopted for the calculations of the jet kinematics.

3.2 Trajectories of the superluminal components

3.2.1 The fits

For each component we derive a polynomial fit to the component offsets $x(t)$, $y(t)$ from the position of the core D. Fitting the component coordinate offsets enables subsequent reconstruction of the time evolution of the component two–dimensional trajectories. The functional form of the fits

$$\mathcal{F} = \sum_{i=0,N}^{N} a_i (t - t_0)^i \tag{3.1}$$

is referred to the epoch $t_0 = 1986.0$, which is approximately in the middle of the overall time span covered by the VLBI monitoring. The order N of the polynomial fits is selected for each component individually, so the fits adequately represent the observed bends in the trajectory. For each component, we also introduce an ad hoc epoch of origin τ_0 such that the component trajectories go through the point $x(\tau_0) = y(\tau_0) = 0$.

Normally, we fit the data at different frequencies together, neglecting possible frequency dependent shifts of the VLBI core position (Königl 1981). Because most of the components are fairly extended and are relatively far away from the core, the expected shifts are within the measurement errors, and therefore they cannot significantly affect the fits at different frequencies. For the components within about 1 mas separation from the core, the position shift can become a significant factor. Because of this effect, we use only the data at 22 GHz, to determine the kinematic properties of C7, the closest and the youngest component. For C6, we correct the component positions at 5 and 8 GHz for the expected shift of the core, before calculating the component trajectory. The effect and implications of the frequency dependent shift of the VLBI core will be discussed in more detail in Chapter 4.

The fitted polynomial coefficients are given in Table 3.1, for each jet component. The order of the fitted polynomials vary from the second (C1, C2) to the fifth (C4, C5), depending on the complexity of the component trajectories.

3.2.2 Trajectories

Based on the available data, we can divide the jet component into three groups: 1) the outermost components, C1, C2, C3 (observed at 4–20 mas separations from the core); 2) the intermediate components, C3, C3a, C4, C5 (the main bulk of data corresponds to 1–4 mas separations); 3) the close components C6, C7 (mostly observed at separations smaller than 1 mas). These three groups describe typical behavior of the jet at different spatial scales. C3 is included in both the outer jet and the intermediate jet, because it was observed at separations ranging from 1 to almost 10 mas. In its kinematic properties, C3 is closer to the successive components C3a and C4.

3.2.3 Outer jet

The components found at separations larger than 4 mas are likely to have almost straight trajectories. However, possible deviations from a straight line cannot be ruled out by the observations, because of the large position errors and poor time sampling of the available VLBI data.

Table 3.1: Polynomial fits to the component trajectories.

Comp.	a_0	a_1	a_2	a_3	a_4	a_5	τ_0
C1							1960.0
$x(t)$	0.15044e+02	0.28518e+00	-0.11249e-01				
$y(t)$	0.84938e+01	0.34221e+00	0.55623e-03				
C2							1968.0
$x(t)$	0.63645e+01	0.42678e+00	0.41162e-02				
$y(t)$	0.21115e+01	0.17320e+00	0.30963e-02				
C3							1976.0
$x(t)$	0.33463e+01	0.40358e+00	0.23719e-01	0.16345e-02			
$y(t)$	0.58256e+00	0.14516e+00	0.16068e-01	0.72770e-03			
C3a							1977.5
$x(t)$	0.18365e+01	0.23879e+00	0.26098e-01	0.27470e-02			
$y(t)$	0.11701e+00	0.82452e-01	0.12169e-01	0.68236e-03			
C4							1979.0
$x(t)$	0.11767e+01	0.23207e+00	0.29010e-01	0.65358e-02	-0.60834e-04	-0.86395e-04	
$y(t)$	0.16385e+00	-0.44512e-01	0.20175e-02	0.84626e-02	0.28539e-03	-0.10849e-03	
C5							1980.0
$x(t)$	0.60975e+00	0.14821e+00	0.18378e-01	0.16814e-02	-0.14932e-03	-0.21677e-04	
$y(t)$	-0.20126e+00	-0.96796e-01	0.62012e-02	0.18212e-02	-0.13097e-03	0.55885e-05	
C6							1987.5
$x(t)$	-0.70719e+00	0.55283e+00	-0.56112e-01	0.18481e-02			
$y(t)$	0.11444e+00	-0.82139e-01	0.55349e-02	0.10695e-03			
C7							1988.0
$x(t)$	0.16654e+00	-0.27944e+00	0.14968e+00	-0.29978e-01	0.21007e-02		
$y(t)$	-0.42487e+00	0.48187e+00	-0.18940e+00	0.30950e-01	-0.17871e-02		

Notes: τ_0 is the epoch of zero-separation (epoch of "origin").

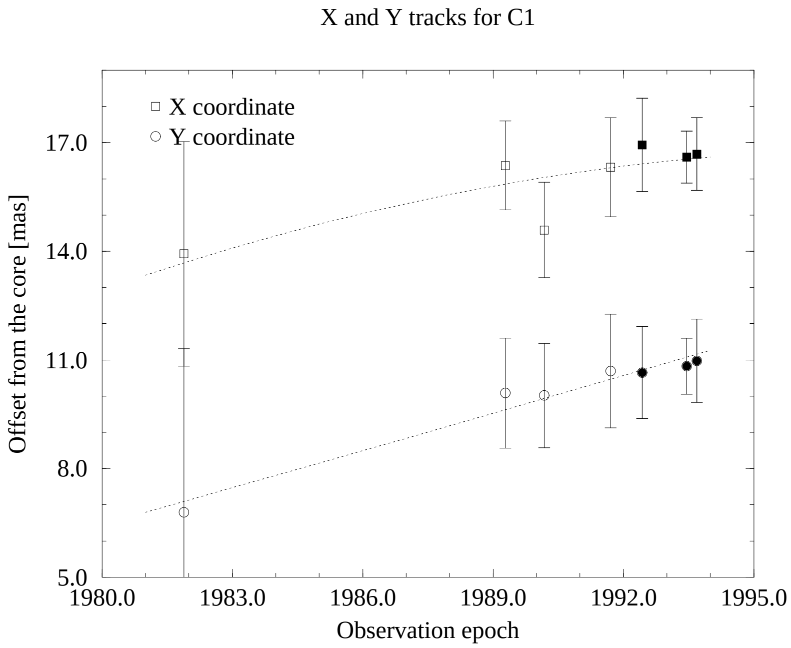

Figure 3.1: Polynomial fits to the relative positions $x(t)$, $y(t)$ of C1. Filled symbols indicate the measurements made for this dissertation.

C1

In the images made for the epochs later than 1989, C1 is identified with the outermost component of the jet. It was detected by Unwin and Wehrle (1992) at 5 GHz (epoch 1989.25) at the distance of about 19 mas. The earliest available detections of C1 are dated back to 1981.78 (Waak *et al.* 1988) and 1981.89 (Biretta *et al.* 1986).

The overall kinematic data consist of 7 position measurements made at 2.3 and 5 GHz. The coordinate offsets and polynomial fits are presented in Figure 3.1. Figure 3.2 shows the corresponding component trajectory in the picture plane. The trajectory is nearly straight. In 13 years, the direction of component motion had changed by about 10°. In 1994, according to the fit, the two–dimensional velocity vector of C1 is consistent with the large–scale jet position angle ($\phi \approx -40°$ measured North–through–East). The fitted trajectory shows a decrease of the component proper motion from 0.52 mas/year to 0.36 mas/year. The latter value gives $\beta_{app} = 7.2h^{-1}$, which is consistent with estimates made by Unwin and Wehrle (1992). Thus, C1 remains a superluminal feature at the observed distance of about $80(h\,\sin\theta)^{-1}$ pc. The actual distance travelled by the shock from 1981 to 1993 is small. In a curved jet with constant Lorentz factor $\gamma_{shock} = 10$, C1 would have moved for about $5h^{-1}$ pc. (The estimate of Lorentz factor $\gamma = 10$ gives the most likely value of Lorentz factor derived from kinematic considerations (see Zensus, Cohen, and Unwin 1995). The details of kinematic calculations in the jet frame are discussed in Section 3.3.1.)

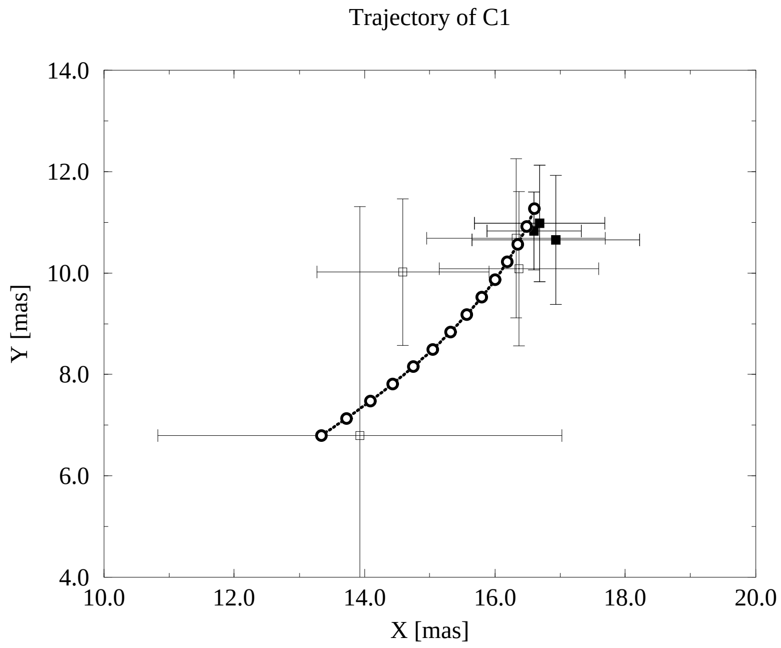

Figure 3.2: Two–dimensional trajectory of C1. Dotted line is reconstructed from the polynomial fits to the component relative positions. White circles show the changes of component position with an interval of 1 year.

C2

C2 is regularly detected in the jet of 3C345 from 1979 to 1989. Later, its brightness becomes too low, when the component distance from the core has exceeds 9 mas. The region of the jet within ≈9–12 mas distance from the core exhibits a decrease of emission that was also noted by Unwin and Wehrle (1992). The decreased emissivity may be a result of increased viewing angle, or jet decollimation. Because of this effect, we have been able to detect the C2 emission only in the 1992.45 5 GHz map which has a substantially increased dynamic range.

The polynomial fits to the component coordinate offsets from the core are given in Figure 3.3. The fits are nearly straight, indicating that there were no significant changes in component velocity. The component trajectory plotted in Figure 3.4 confirms this conclusion. A slight acceleration shown in the fit for the latest epochs can be caused by insufficient data and increasing errors in position measurements.

The component apparent velocity changes from $\beta_{app} = 8.5h^{-1}$ in 1983.0 to $\beta_{app} = 10.4h^{-1}$ in 1993.0.

3.2.4 Intermediate jet

On the intermediate scales (1–4 mas), the jet components are expected to have curved trajectories and substantial variations of velocity. The locations, fluxes and sizes of

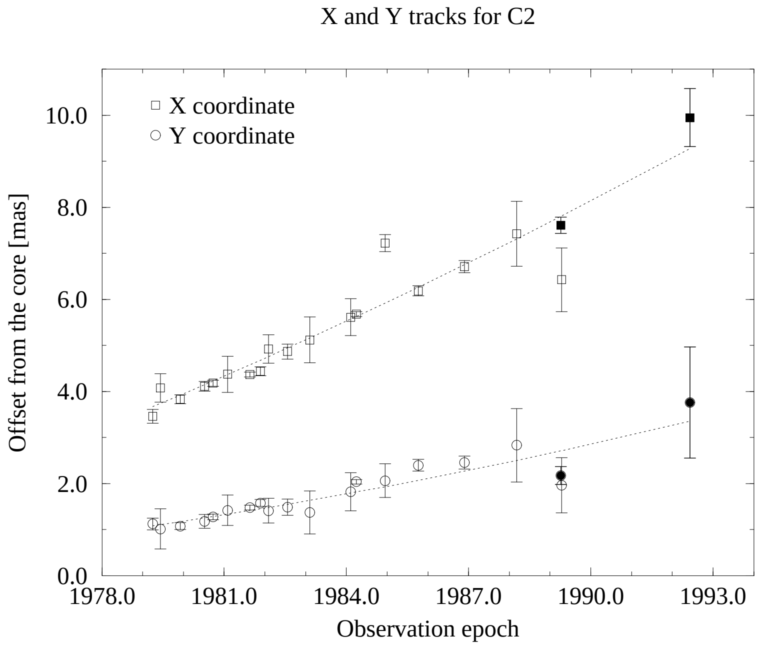

Figure 3.3: Polynomial fits to the relative positions $x(t)$, $y(t)$ of C2. Filled symbols indicate the measurements made for this dissertation.

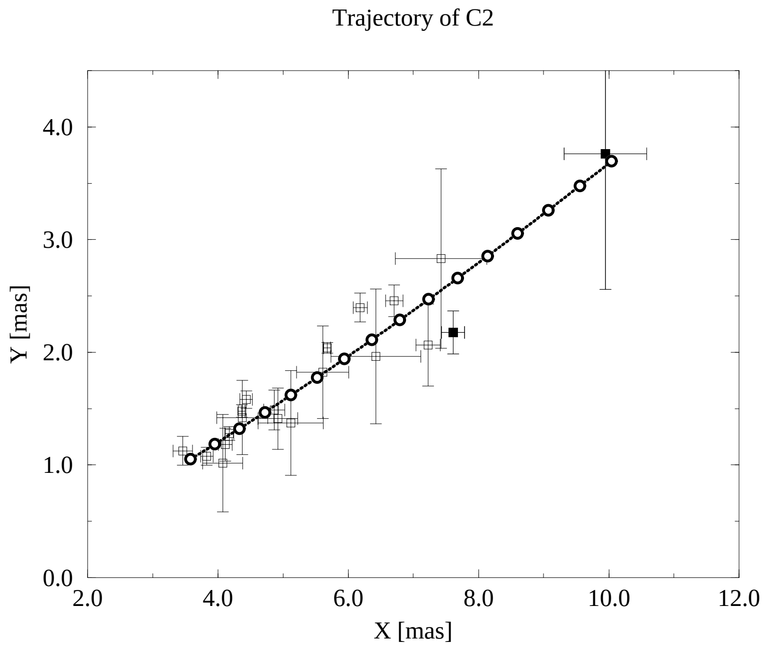

Figure 3.4: Two–dimensional trajectory of C2. Dotted line is reconstructed from the polynomial fits to the component relative positions. White circles show the changes of component position with an interval of 1 year.

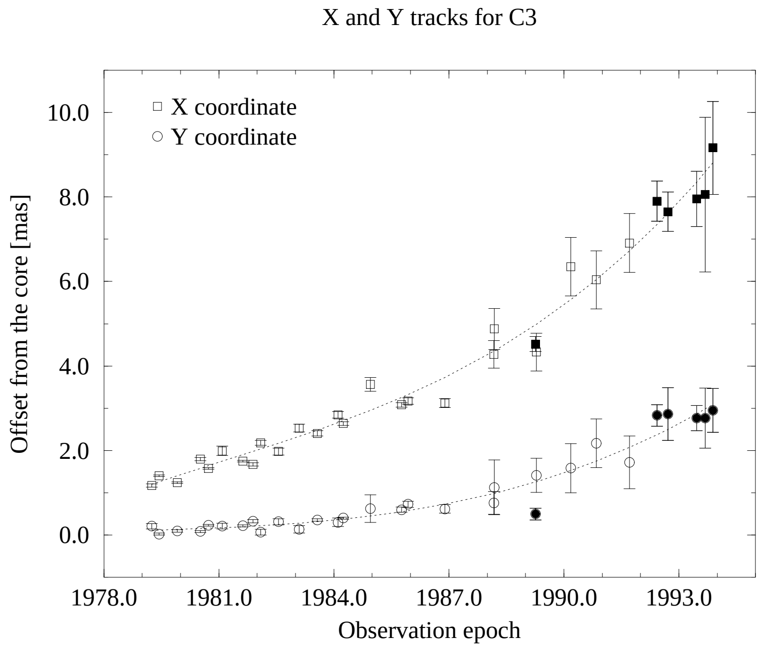

Figure 3.5: Polynomial fits to the relative positions $x(t)$, $y(t)$ of C3. Filled symbols indicate the measurements made for this dissertation.

the components are determined most reliably, at these scales.

C3

C3 is well detected over the whole time of monitoring. The measured positions are consistent, and show a substantial curvature of the component coordinate offsets from the core (Figure 3.5). Increasing errorbars at the epochs later than 1988 are due to lower flux density and larger size of the component at these epochs.

The corresponding trajectory plotted in Figure 3.6 becomes a straight line, when the component distance from the core exceeds 4 mas. At closer distances, the direction of the component motion changes from $\phi_{1979} = -85°$ to $\phi_{1986} = -70°$. After the trajectory becomes straight, the component accelerates visibly, changing its apparent speed from $\beta_{app} = 8.5h^{-1}$ in 1986.0 to $\beta_{app} = 18.9h^{-1}$ in 1992.0.

C3a

The identifications of C3 and C4 were made shortly after an outburst occured in 1979. At later epochs, a weaker feature was found between C4 and C3. In order to preserve the naming convention, the newly discovered feature was named C3a. At 22 GHz the flux of C3a never reached 0.5 Jy, and it was visible at 10.7 and 5 GHz predominantly. The weakness of C3a, and its closeness to C4, raise the question about a possible relation between these two components. C3a may have originated from a split in

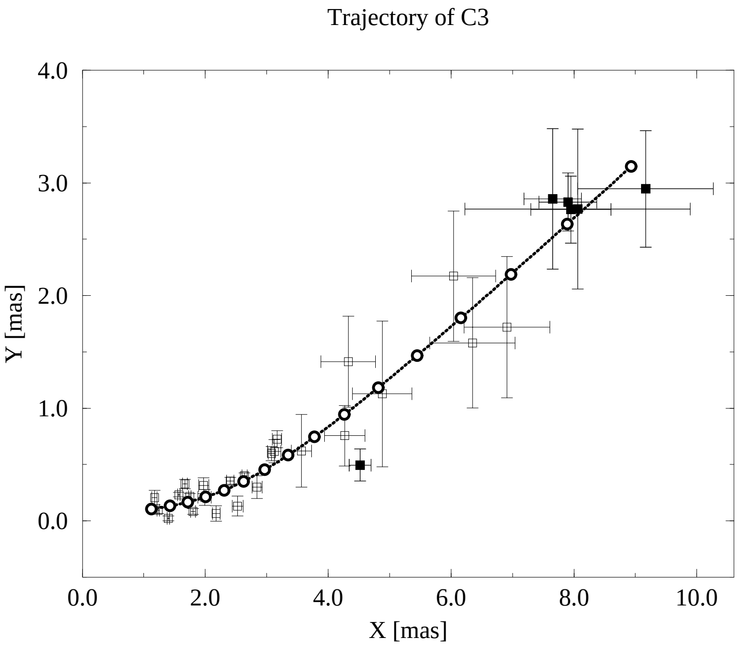

Figure 3.6: Two–dimensional trajectory of C3. Dotted line is reconstructed from the polynomial fits to the component relative positions. White circles show the changes of component position with an interval of 1 year.

C4 due to passage of the latter through a recollimation shock. A similar effect was observed in the simulations of relativistic jets made by Gòmez *et al.* (1995).

In our observations, C3a can be identified in only one image (1989.26, at 10.6 GHz). The combined data consist of 12 epochs covering the time period from 1979 to 1992. At the most recent epochs, identifications of C3a are impeded by its decreasing surface brightness. We were unable to segregate the emission from C3a in the 5 GHz maps made in 1992 and 1993. The latest identification of C3a is made in the image from September 1991 (taken from Unwin and Wehrle, 1992).

The polynomial fits to the component coordinate offsets from the core are shown in Figure 3.7. Because the measurements are distributed sparsely in time and made at different frequencies, we do not attempt to force the fit to go through every point, but choose a third order polynomials to account for the general trend. The trajectory corresponding to the polynomial fits is shown in Figure 3.8. It is seen in Figure 3.8 that at separation of about 1 mas C3a turns from $\phi = -86°$ to $\phi = -70°$, almost identical to the turn observed in C3. After that, the component accelerates, reaching $\beta_{app} \approx 16h^{-1}$ in 1991.50.

C4

C4 is the most prominent and well–studied feature in the jet. The component trajectory was modeled by a helix (Steffen *et al.* 1995); the emission properties are

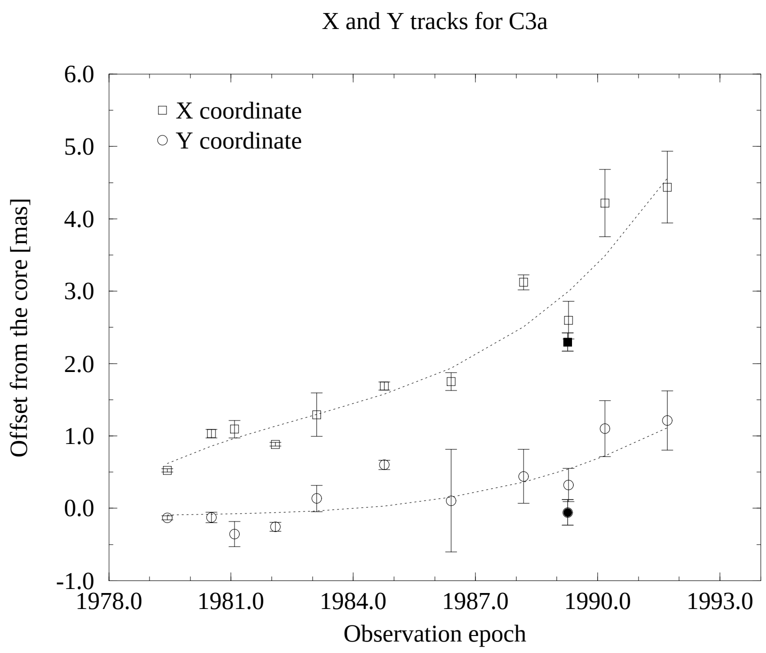

Figure 3.7: Polynomial fits to the relative positions $x(t)$, $y(t)$ of C3a. Filled symbols indicate the measurements made for this dissertation.

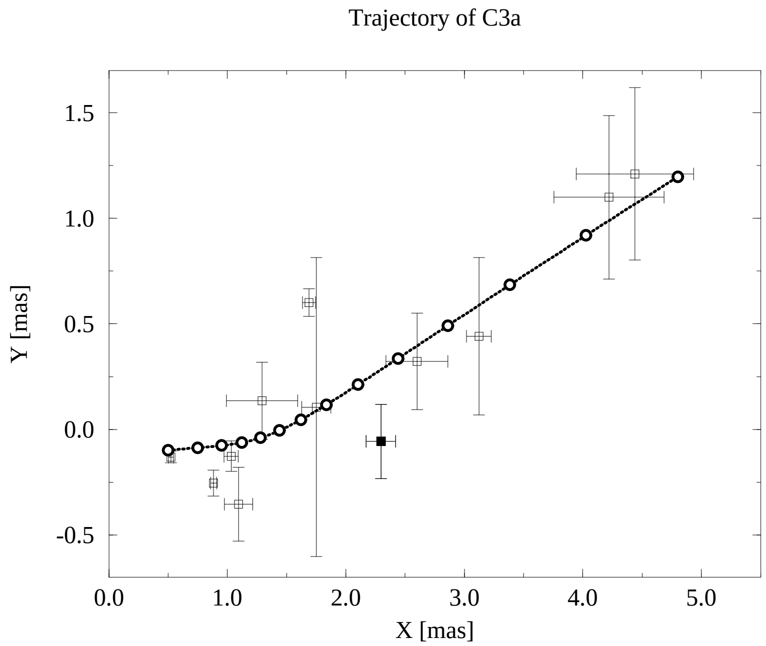

Figure 3.8: Two–dimensional trajectory of C3a. Dotted line is reconstructed from the polynomial fits to the component relative positions. White circles show the changes of component position with an interval of 1 year.

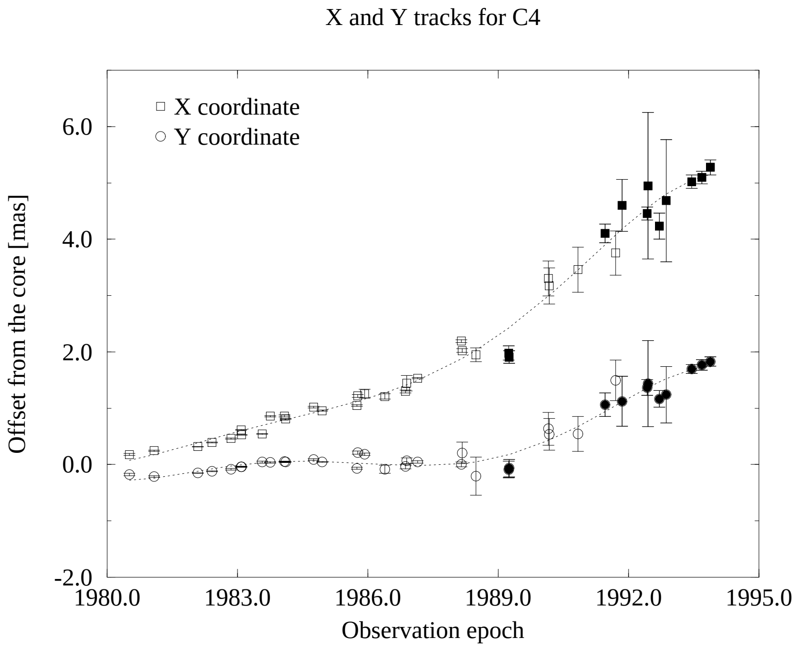

Figure 3.9: Polynomial fits to the relative positions $x(t)$, $y(t)$ of C4. Filled symbols indicate the measurements made for this dissertation.

discussed by Rabaça and Zensus (1994). In our data, the detections are made for C4 over the entire monitoring period, and the data cover the component evolution from the early stages on. The results of polynomial fitting to the component coordinate offsets from the core are shown in Figure 3.9. Both $x(t)$ and $y(t)$ fits show substantial curvature; a decrease of $y(t)$ between 1984 and 1988 is well justified by the amount and consistency of the data from these epochs. The corresponding two–dimensional path of C4 plotted in Figure 3.10 shows a remarkably well–defined twist present in the component trajectory. At distances closer than 0.5 mas and larger than $\approx$3.5 mas C4 moves to the same direction ($\phi \approx -60°$). The observed twist may reflect the helical nature of the C4 trajectory. The apparent speed of C4 reaches $\beta_{app} = 16h^{-1}$, in 1992.0.

C5

C5 was first detected in 1983.09, and is present in most of the images, with the exception of the latest 22 GHz epochs. The component is significantly weaker than C4, and follows a distinctively different evolution.

The polynomial fits to the coordinate offsets of C5 from the core are shown in Figure 3.11. Consistency of the position measurements facilitates the fitting. The $x(t)$ curve appears to be similar to that of C4. The $y(t)$ curve shows a deep decrease down to about -0.5 mas. The peculiarity of this curve is reflected in the reconstructed trajectory of C5 plotted in Figure 3.12 The trajectory of C5 differs from the trajectories

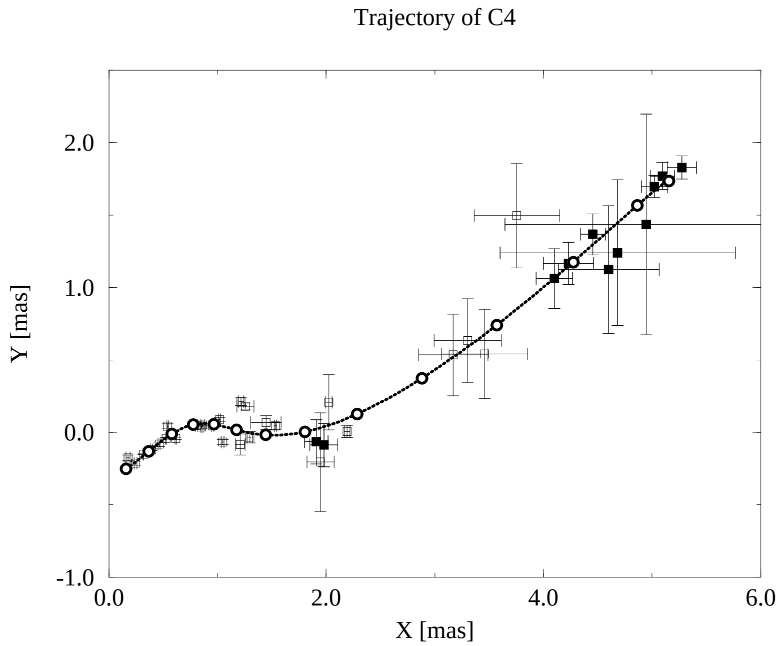

Figure 3.10: Two–dimensional trajectory of C4. Dotted line is reconstructed from the polynomial fits to the component relative positions. White circles show the changes of component position with an interval of 1 year.

of all preceeding components. However, additional data are required, in order to find an explanation for this difference. It is also possible that C5 will follow the common path, with increasing distance from the core. In 1993 C5 was moving in the direction of $\phi = -63^{\circ}$ which is similar to the motions of the preceeding components. The component was moving at $\beta_{app} = 4.7$, and was decelerating. The maximum apparent velocity $\beta_{app} = 6.3$ was achieved in 1990.9. This value is considerably lower than the velocities of the preceeding components, which may explain the comparably lower flux density of C5 at all frequencies.

3.2.5 Inner jet

The most recent observations have revealed the appearances of two new superluminal features, C6 and C7. After the appearance of C5, the source was in a quiescent stage for about 5 years. C6 and C7 were first detected at 100 GHz at the epochs of 1988.2 and 1989.2, respectively (Krichbaum *et al.* 1991). The earliest detection at 22 GHz is made at the epoch of 1989.25 (this dissertation). The data accumulated for C6 and C7 enables a study of the earliest stages of component kinematic evolution within 1 mas from the core.

C6

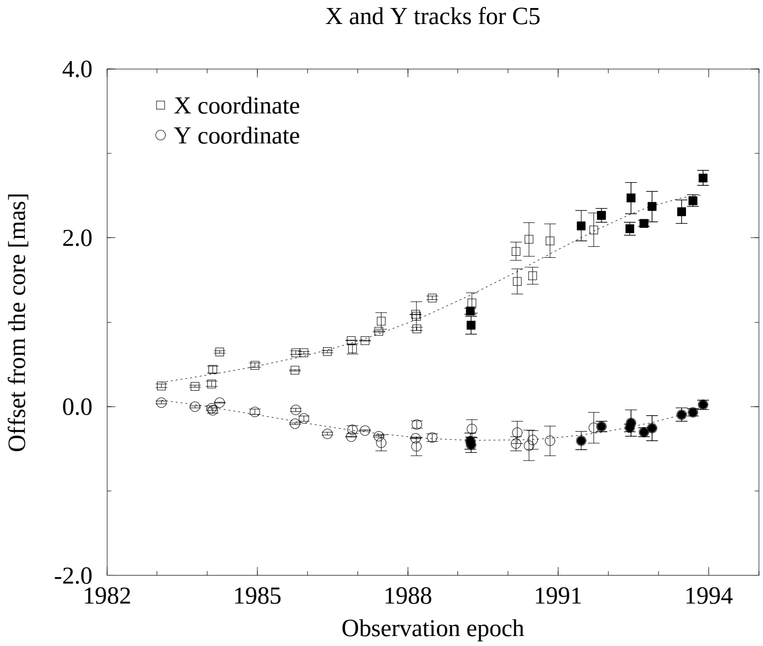

Figure 3.11: Polynomial fits to the relative positions $x(t)$, $y(t)$ of C5. Filled symbols indicate the measurements made for this dissertation.

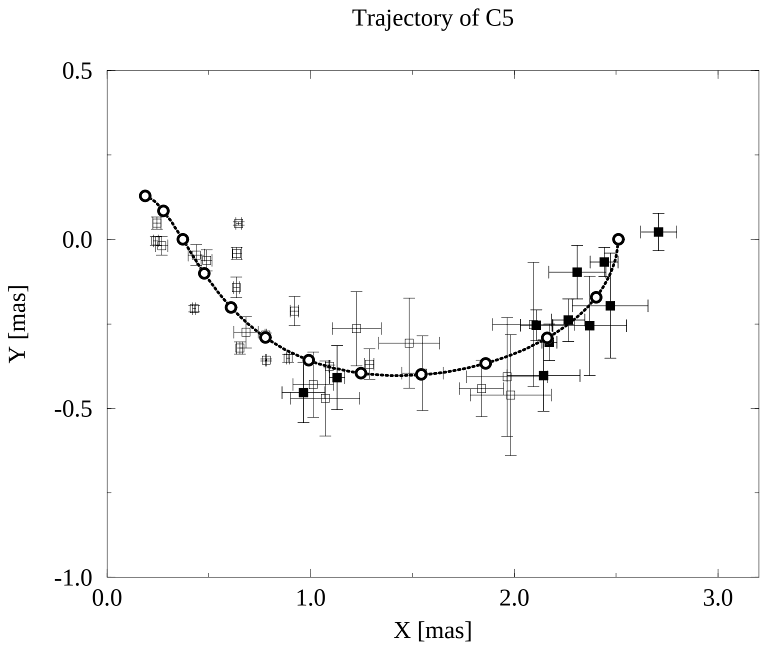

Figure 3.12: Two–dimensional trajectory of C5. Dotted line is reconstructed from the polynomial fits to the component relative positions. White circles show the changes of component position with an interval of 1 year.

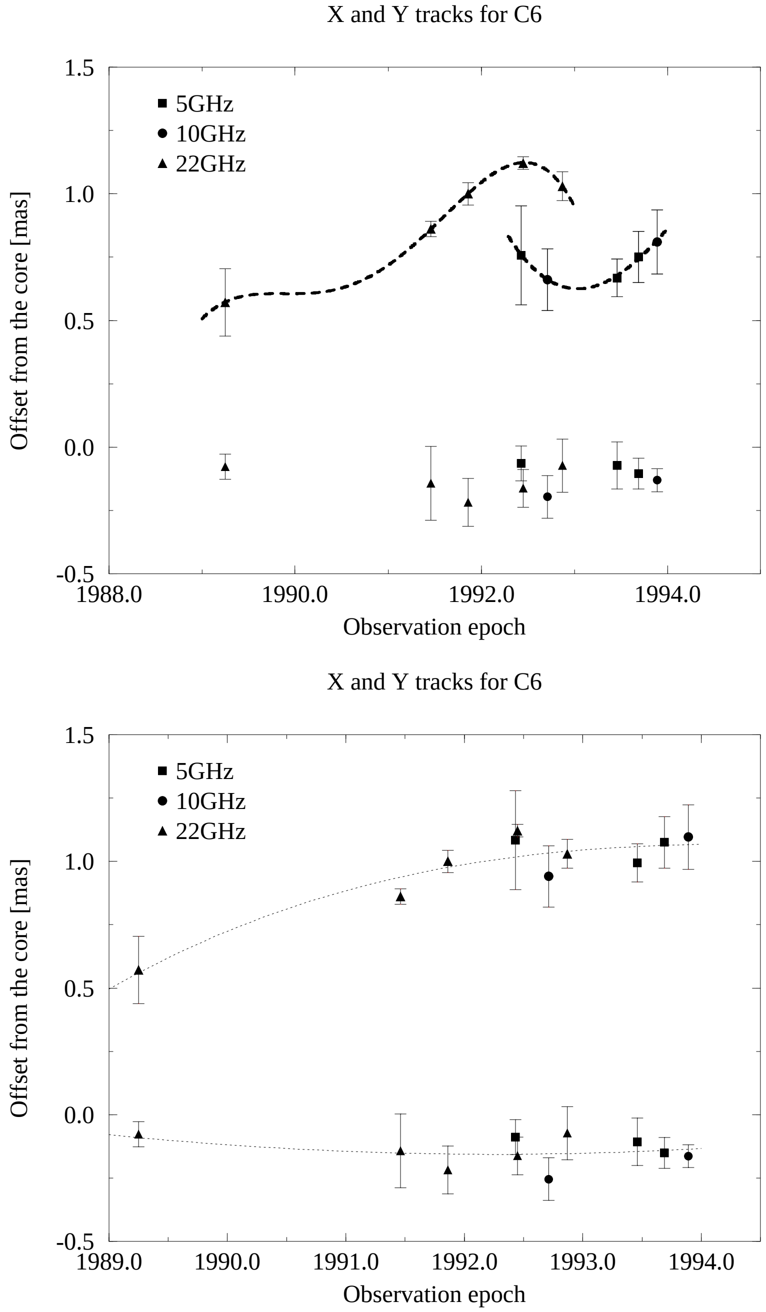

Figure 3.13: Polynomial fits to the relative positions $x(t)$, $y(t)$ of C6. Filled symbols indicate the measurements made for this dissertation. Top panel shows actual data points and separate fits to the $x(t)$ data at 22 GHz (triangles), and at 5 and 11 GHz (squares and circles). The bottom panel gives the component positions corrected for the frequency dependent shift of the core position, and shows the polynomial fit to all data combined.

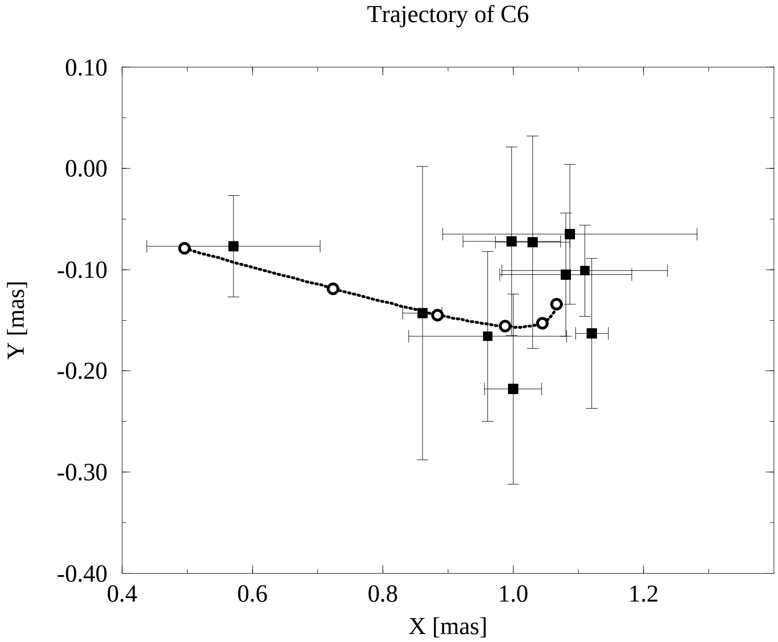

Figure 3.14: Two–dimensional trajectory of C6. Dotted line is reconstructed from the polynomial fits to the component relative positions. White circles show the changes of component position with an interval of 1 year.

For the fitting of the C6 trajectory, we do not use the observations made at 43 and 100 GHz. One of the reasons for this is that the positions obtained from VLBI images at such high frequencies are, generally, not very reliable. The main reason to abandon the high frequency data is the frequency dependent shift of the core position (Königl 1981) resulting in systematic offsets of the component positions measured at different frequencies. We discuss this effect in Section 4.2.3 of Chapter 4. In that section, we determine the relative offsets between the component positions measured at 5, 8, 11, and 22 GHz. Since there are no appropriate data available at higher frequencies, the frequency dependent shift cannot be measured or corrected, at those frequencies. Therefore, we leave out the observations made at 43 and 100 GHz.

The effect of a frequency dependent shift can be illustrated by Figure 3.13. In the top panel, the x coordinate data at 22 GHz differ significantly from the data at lower frequencies. The fit to the data at all three frequencies results in very peculiar and abrupt changes of the component trajectory and velocity.

In the bottom panel of Figure 3.13, the component positions at 5 and 8 GHz are corrected for the position offsets with respect to the positions at 22 GHz. After the correction is applied, it is possible to obtain a satisfactory fit. However, the time gap between 1989.25 and 1991.45 seen in the data is likely to undermine the fit for this time period.

The resulting trajectory of C6 plotted in Figure 3.14 shows a nearly straight path. Apparently, C6 was decelerating, from 1991 on. We cannot draw conclusions on the velocity changes at earlier epochs, since the available data are not sufficient for adequate fitting at those epochs. The deceleration of C6 is consistent with the flux and size changes of the component (see Chapter 5 for discussion of the long–term evolution of the jet). In 1993, C6 could not be detected at 22 GHz, when its separation from the core barely exceeded 1 mas. (In comparison: the last detection of C4 was made at 22 GHZ, at 4.8 mas separation from the core). Such rapid decay of the 22 GHz emission of C6 can be explained either by the internal weakness of C6, or by unfavorable geometrical conditions of its trajectory. In view of these possibilities, the sharp turn observed in the reconstructed trajectory of C6 at the epochs 1992.8-1994.0 may be consistent with the rapid flux decrease.

According to the fit, C6 became subluminal in 1992.7, and reached its minimum apparent velocity $\beta_{app} = 0.5h^{-1}$, in 1993.7. For an approaching component, subluminal speeds can be observed if the component moves at a viewing angle θ with the line of sight such that

$$1 \geq \cos\theta > \frac{1}{\beta}\left[1 + \left(2\beta^2 - 1\right)^{0.5}\right], \tag{3.2}$$

where β is the component speed. For C6, moving with $\gamma = 10$, this angle should be as small as $0.2°$ to explain the minimum apparent velocity in 1993.7.

C7

C7 is a considerably stronger feature compared to C6. The sufficiently large amount and good quality of the data at 22 GHz allow us to avoid using observations at other frequencies for fitting the component trajectory. This eliminates, effectively, the uncertainties related to handling the frequency dependent shift of the component relative position. The closeness of C7 to the core makes this component a unique source of information about the jet kinematics in the immediate vicinity of the jet origin.

The polynomial fits to the component coordinate offsets from the core are shown in Figure 3.15. It is seen in Figure 3.15 that the position of C7 did not change significantly from 1989.2 to 1991.5. Later, significant changes occur in both $x(t)$, and $y(t)$, that indicate the presence of a strong acceleration and a sharp turn in the component trajectory. The reconstructed trajectory plotted in Figure 3.16 confirms these conclusions. A 90° turn is seen in the fitted curve. The presence of such turn is required, from the fits to the component's coordinate offsets $x(t)$ and $y(t)$. At later epochs, the curve shows a considerable acceleration resulting in the observed apparent velocity $\beta_{app} = 9.4h^{-1}$, in 1993.5. The fit suggests that between 1989.2 and 1991.5 C7 remained a subluminal feature. Similar to the case of subluminal motion in C6, we cannot rule out the possibility of measurement errors that could affect the derived velocity. However, the derived velocity changes are consistent with the initial stages of component evolution as predicted by the two–fluid model (Roland *et al.* 1994).

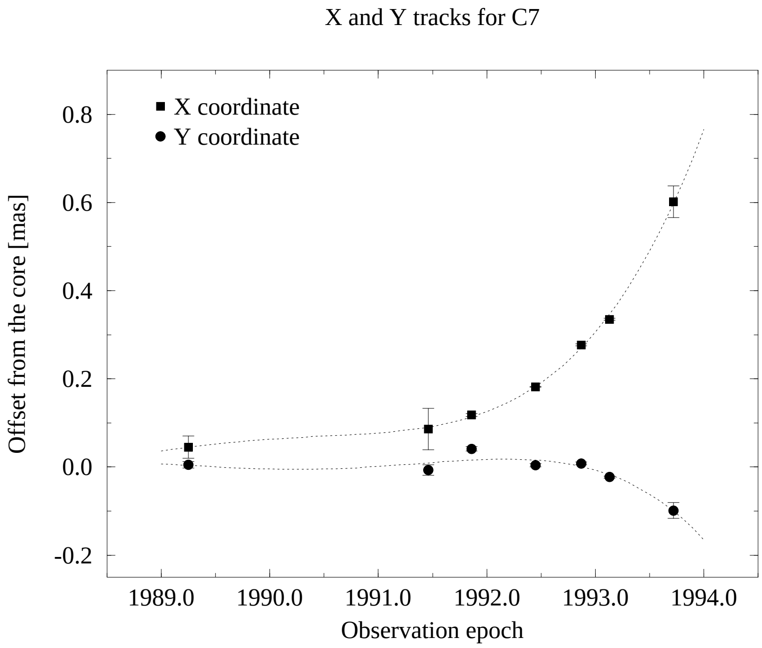

Figure 3.15: Polynomial fits to the relative positions $x(t)$, $y(t)$ of C7. Filled symbols indicate the measurements made for this dissertation.

3.2.6 Component tracks

In Figure 3.17, the two–dimensional trajectories of all components are plotted together, to illustrate the general outline of the jet. It is remarkable that the trajectories of different components are similar, indicating that the jet is well–collimated and steady over substantially large spatial and time scales. The gap seen at 10–14 mas separation from the core corresponds to the low–brightness region of the jet where position measurements have so far not been possible. The trajectory of C1 lies approximately on a continuation of the tracks of the closer components, indicating that there are no significant changes occuring in the jet up to 20 mas separation from the core. Curvature seen in the trajectory of C1 provides evidence for the transition from the compact jet ($\phi \approx -70°$) to the large–scale jet ($\phi \approx -40°$, see Kolgaard *et al.* 1989). The sharp increase of the jet width observed in C1 suggests changing physical conditions of the jet (possibly due to adiabatic expansion). Thus, these two facts can provide us with an estimate of the extent of the compact jet in 3C345. From the position of C1 at which it begins to move with $\phi = -40°$, the extension of compact jet is approximately $80(h\,\sin\theta)^{-1}$ pc.

From the viewpoint of kinematic models (the helical motion model, in particular), the crucial changes in component trajectories must occur very close to the beginning of the component evolution. The limited resolution of our data (in both spatial and time domains) does not enable a detailed study of fine changes of the component trajectories occuring within 1 mas separation from the core. It is seen in the plot

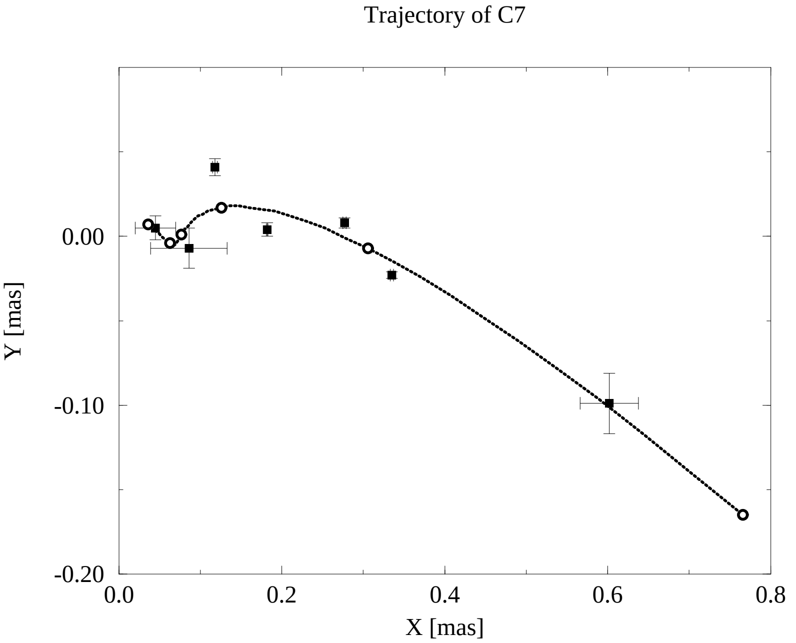

Figure 3.16: Two–dimensional trajectory of C7. Dotted line is reconstructed from the polynomial fits to the component relative positions. White circles show the changes of component position with an interval of 1 year.

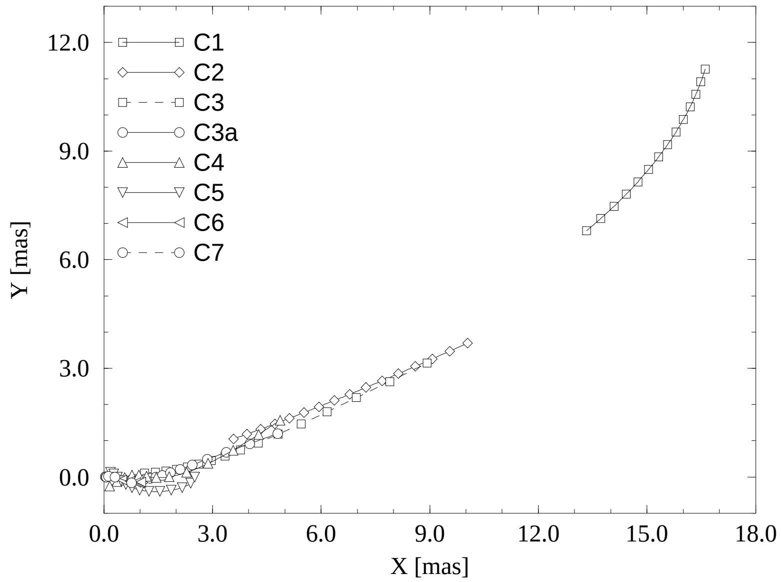

Figure 3.17: Fitted trajectories of the jet components.

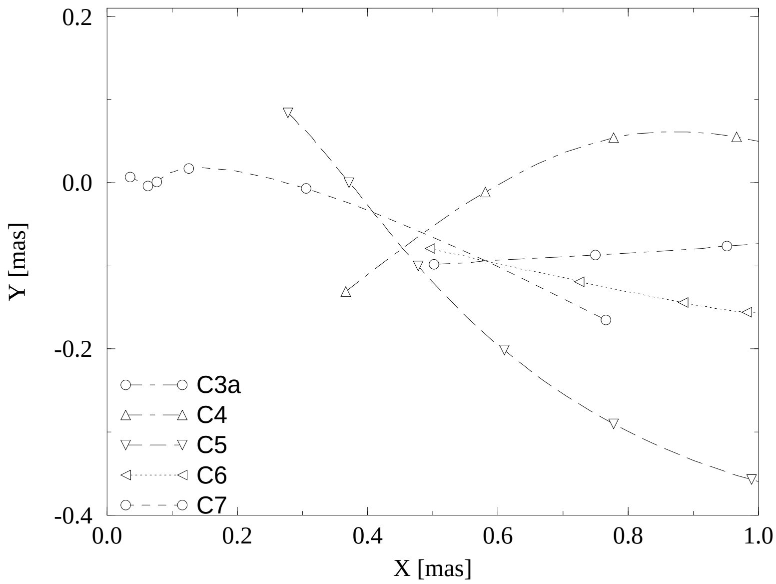

Figure 3.18: Fitted trajectories of the jet components at separations smaller than 1 mas.

presented in Figure 3.18 that only the trajectory of C7 can be traced closer than 0.3 mas distance from the core. The shape of the curve for C7 suggests that it would require extensive data within 0.2 mas, in order to select the most suitable kinematic scenario.

Another interesting feature in Figure 3.18 is the region around (x=0.5, y=-0.1). The trajectories of all components (with exception of C1 and C2 which were never observed so close to the core) go very close to each other, in the vicinity of the point (0.5,-0.1). The available data is insufficient for making a conclusion as to whether the observed effect is real and reflects the geometry of the jet, or is only a coincidence.

3.3 Kinematics of the jet

In this section, we describe kinematic properties of the superluminal components, and study the kinematic evolution of the jet. In our study, we attempt to minimize the number of a priori model assumptions made about the jet geometry, and therefore we will pay special attention to model independent quantities: proper motions, apparent distances travelled along the jet, and apparent velocities of the jet components.

3.3.1 Calculation of kinematic parameters

To calculate various kinematic parameters of the jet components, we have developed software that analyzes polynomial fits to the component trajectories. The calculated quantities include: 1) proper motion, μ; 2) apparent distance travelled along the jet, Θ_{app}; 3) distance travelled in the rest frame of the source, R; 4) apparent velocity, β_{app}; 5) rest frame velocity, β; 6) angle between the true velocity vector and the line of sight, θ; 6) Doppler factor, δ; 7) Lorentz factor, γ; 8) instantaneous apparent acceleration, β'_{app}; 9) instantaneous rest frame acceleration, β'.

In the "standard" comsological model, the luminosity distance is given by

$$D_L = \frac{c}{H_0 q_0}\left\{q_0 z + (q_0 - 1)[(1 + 2q_0 z))^{1/2} - 1]\right\}, \tag{3.3}$$

which translates into $D_L = 1.99h^{-1}$ Gpc, for 3C345 ($z = 0.594$, Hewitt and Burbidge 1993). Correspondingly: at $z = 0.594$, the angular dimension of 1 mas translates into a $3.79h^{-1}$ pc linear extension; and the proper motion of 1 mas/year results in an apparent velocity of $19.7h^{-1}c$.

Given the polynomials fits $x(t)$, $y(t)$ to the component coordinates offsets, we reconstruct the time evolution of the component proper motion

$$\mu(t) = \left[\left(\frac{dx}{dt}\right)^2 + \left(\frac{dy}{dt}\right)^2\right]^{1/2} \tag{3.4}$$

We then determine the distance travelled by the component along the jet

$$\Theta_{app}(T) = \int_{\tau_0}^{T} \mu(t)dt \tag{3.5}$$

and the component instantaneous apparent velocity

$$\beta_{app}(t) = \mu(t)D_L(1 + z)^{-1} \tag{3.6}$$

Since $\beta_{app}(t) = \beta(t)\sin\,\theta(t)[1 - \beta(t)\cos\,\theta(t)]^{-1}$, we have to make an assumption about either θ or β, in order to calculate kinematic properties of the jet components. To avoid over parameterization of the calculations, we omit the case when both θ and β change along the jet. We also do not restrict the component trajectories to any specific class such us, for instance, *helical motion*. A helical trajectory was calculated for C4 in Steffen *et al.* (1995), to describe the component trajectory. In our calculations we consider two extreme cases of the jet geometry:

Jet with invariant viewing angle

$\theta = const.$

This (rather unrealistic) situation corresponds to a jet moving at constant viewing angle, with the jet rest frame velocity variations responsible for the observed trajectory. The instantaneous rest frame velocity can be deduced from the relation:

$$\beta(t) = \frac{\beta_{app}(t)}{\sin\,\theta + \beta_{app}(t)\cos\,\theta} \tag{3.7}$$

Curved jet

$\beta = const.$

A more plausible assumption explaining the observed trajectories by changes in the direction of jet velocity. In this case, there are two solutions for $\theta(t)$:

$$\cos\ \theta(t) = \frac{\beta_{app}^2(t) \pm [\beta^2(\beta_{app}^2(t)+1) - \beta_{app}^2(t)]^{0.5}}{\beta(\beta_{app}^2(t)+1)} \tag{3.8}$$

The solution with "+" is the *small angle* solution; the one with "–" is the *large angle* solution. The large angle solution fails to explain subluminal motions and rapid changes of component trajectories. This argument makes the small angle solution generally more acceptable. We will return to this argument in the discussion of the shock–in–jet model, in Chapter 5.

Once β and θ are determined, we can use them to calculate the component Doppler factors $\delta = \gamma^{-1}(1-\beta\cos\theta)^{-1}$, and derive the kinematic parameters in the rest frame of the source. Cosmological corrections, relativistic time dilation and aberration effects are included into the calculation. In the most general case of joint variations of β and θ, we have for the traveled distance in the rest frame of the jet

$$R(t) = (1+z)^{-1} \int_{\tau_0}^{t} \frac{\beta(t)}{1-\beta(t)\cos\theta(t)} dt \tag{3.9}$$

The time is still more conveniently measured in the observer's frame, but can be transformed to the jet's rest frame t':

$$\Delta t' = (1+z)^{-1} \int_{\tau_0}^{t} \delta t dt \tag{3.10}$$

The aberration effects are corrected for, using the standard aberration formula

$$\cos\theta'(t) = \frac{\beta(t) - \cos\theta(t)}{1-\beta(t)\cos\theta(t)} \tag{3.11}$$

3.3.2 Kinematic properties of the jet

In this section, we discuss the kinematic solutions for the component motions. We describe the limits imposed by the straight jet and curved jet models on the Lorentz factors and viewing angles of the component three–dimensional trajectories. In the last subsection, we discuss global kinematic evolution of the jet.

Constant viewing angle

A peculiar case of possible kinematic solutions to the observed trajectories is θ =const with changing Lorentz factors. If understood in a strict sense, this condition defines a straight jet, and is unable to account for the observed curvature of component trajectories. A loose interpretation of the invariant viewing angle implies rotational

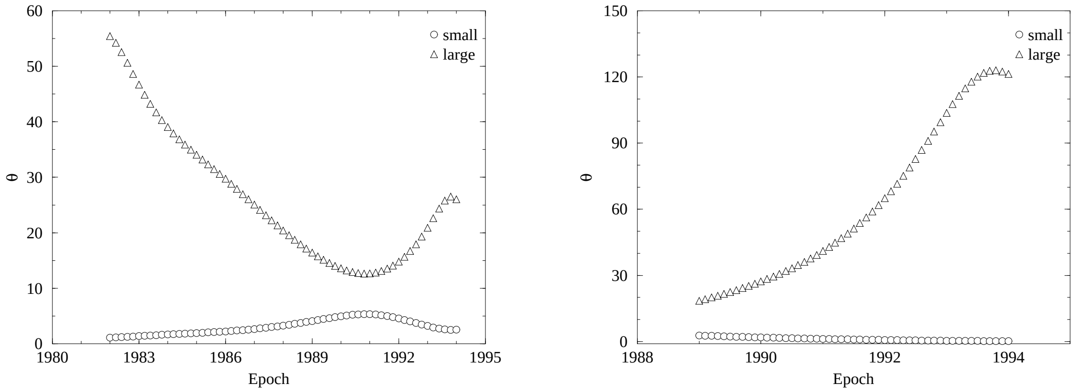

Figure 3.19: Small and large angle solutions for a curved jet with constant Lorentz factor. Solutions are shown for C5 (left panel), and C6 (right panel).

symmetry, and effectively defines a cone with the opening angle θ. A component motion is limited to the surface of the cone. The line of sight coincides with the rotational axis of the cone. In this case, the model is more successful, particularly for the slow moving components C5 and C6. However, for the faster components the Lorentz factor variations are too big. For C3, γ must change from 10 to 50 in order to explain the observed apparent velocity. Such changes of Lorentz factor are hardly acceptable, therefore we do not consider this case in detail.

Small angle solution versus large angle solution

Of the two possible solutions for a curved jet, the small angle solution provides more reasonable ranges of viewing angle. In the large angle solution for the slowest jet components, the viewing angle can even exceed $90°$, implying that the component is receding. Figure 3.19 shows the small and large angle solutions for C5 (left) and C6 (right). The variation of viewing angle is much bigger for the large angle solutions in both components. It is not likely that a jet with such curvature can retain its collimation.

On the contrary, the small angle solution shows variations of viewing angles rarely exceeding $10°$, which can be easily explained by perturbations in a relativistic plasma, or by helical trajectories of the components. Because of these reasons, we use the small angle solution in further analyses of the jet kinematics.

Jet acceleration and viewing angle

The assumptions, γ =const, θ =const, described in Section 3.3.1 provide certain constraints and limitations on the jet kinematics. From the analysis of changes in the apparent velocities of the jet components, it is possible to derive the ranges of kinematic parameters satisfying these constraints, and make general conclusions

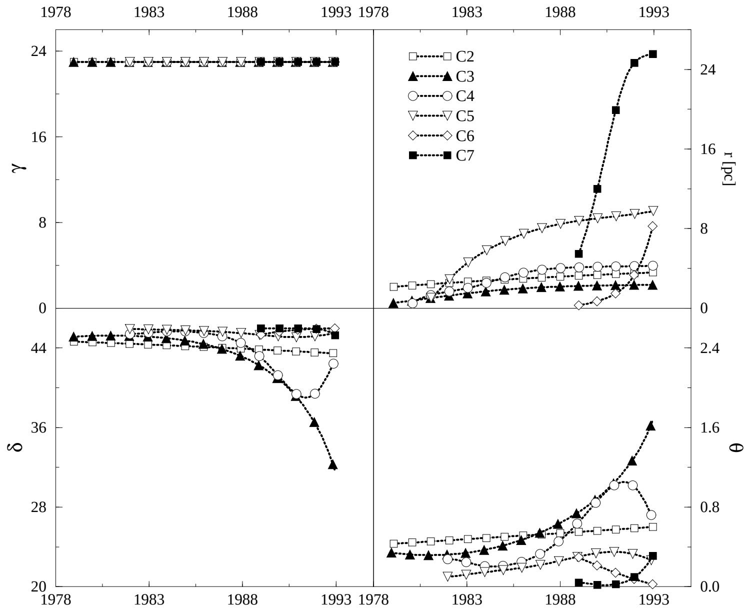

Figure 3.20: Evolution of the component kinematic parameters in the jet moving at constant $\gamma = 23$. The variations of the Lorentz factor (upper left), Doppler factor (lower left), traveled distance in the jet rest frame (upper right), and viewing angle (lower right) are shown.

Table 3.2: Kinematic limits of the component motion

Comp.	Curved jet	Straight jet
C1	$\gamma > 10.3$	$0 < \theta < 11.0°$
C2	$\gamma > 10.7$	$0 < \theta < 10.7°$
C3	$\gamma > 22.9$	$0 < \theta < 5.0°$
C3a	$\gamma > 19.4$	$0 < \theta < 5.9°$
C4	$\gamma > 9.8$	$0 < \theta < 11.7°$
C5	$\gamma > 6.4$	$0 < \theta < 18.0°$
C6	$\gamma > 5.0$	$0 < \theta < 23.0°$
C7	$\gamma > 11.2$	$0 < \theta < 10.2°$

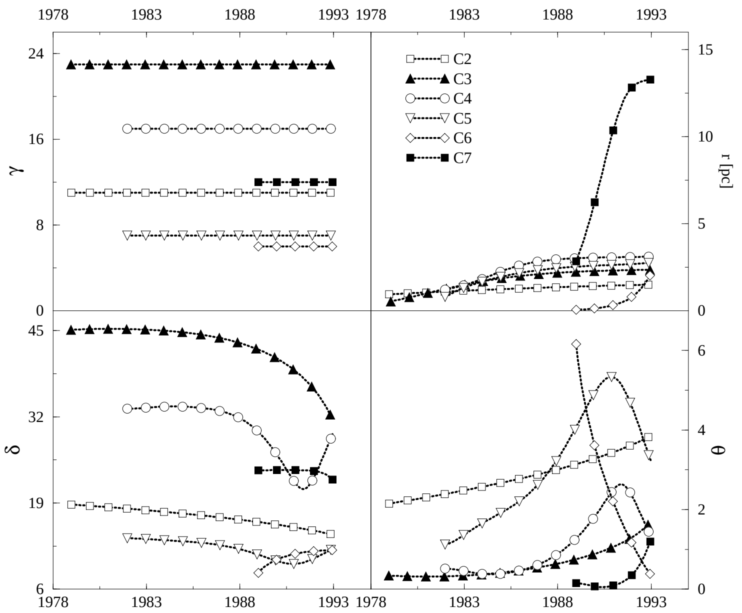

Figure 3.21: Evolution of the component kinematic parameters in the jet moving at constant Lorentz factors, differing for each component. The variations of the Lorentz factor (upper left), Doppler factor (lower left), traveled distance in the jet rest frame (upper right), and viewing angle (lower right) are shown.

about the kinematic properties of the jet.

If the jet Lorentz factor γ is constant, and the observed trajectories are determined by changes of the viewing angle solely, then at any time the inequality

$$\gamma \geq (1+\beta_{app})^{0.5} \tag{3.12}$$

must be observed. Similarly, if θ =const, and the jet curvature is determined by changing Lorentz factor, the range of viewing angles that can provide valid kinematic solutions is:

$$0 \leq \sin\,\theta \leq \frac{2\beta_{app}}{1+\beta^2_{app}} \tag{3.13}$$

The lowest allowed Lorentz factors and limit ranges of allowed viewing angles are summarized in Table 3.2 for all components. The lower limits of Lorentz factors vary from 5.0 for C6 to 22.9 for C3. In order to account for this difference, we have to resort to one of the three possible schemes:

1) All of the component Lorentz factors are constant and equal. This implies that the Lorentz factors of all components must exceed $\gamma = 22.9$, to satisfy the kinematic requirements. The bulk Lorentz factors of the compact jets are not expected to be higher than $\gamma \approx 20$ (Abramovitz 1992; Henri and Pelletier 1992). This limit is not so strict if the observed speed correspond to the shock pattern speeds rather than to a true bulk motion. Even so, it would be rather problematic to explain the formation of

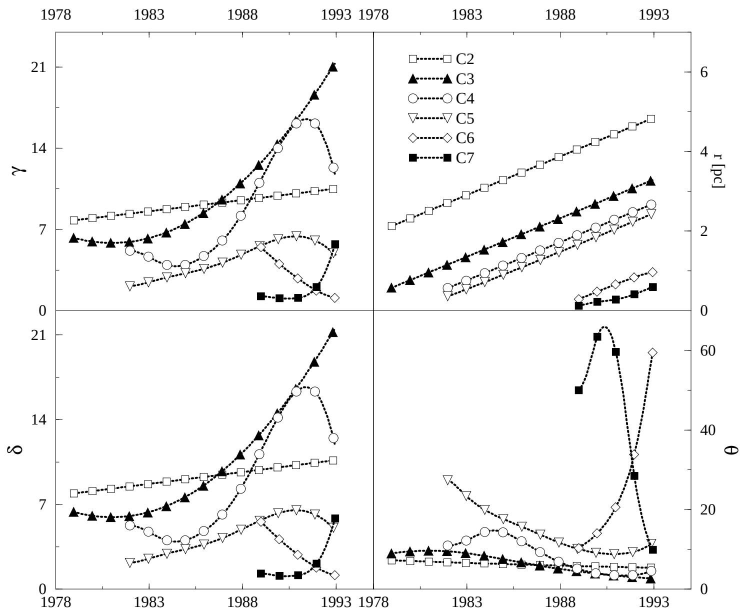

Figure 3.22: Evolution of the component kinematic parameters in the jet with component moving along the trajectories satisfying the minimum kinematic power condition $\gamma_j = (1+\beta_{app})^{0.5}$. The variations of the Lorentz factor (upper left), Doppler factor (lower left), traveled distance in the jet rest frame (upper right), and viewing angle (lower right) are shown.

such fast shocks. Kinematically, this scheme also does not appear to be viable. The evolution of the component Doppler factors, viewing angles and traveled distances is shown in Figure 3.20. In order to be accommodated into the $\gamma_j = 23$ scheme, the trajectory of C6 must have an extremely small viewing angle, $\theta = 0.1 - 0.5°$, and very large length, $R \approx 8\,\mathrm{pc}$, in the rest frame of the source. The distance traveled by C7 must exceed the traveled distance of all the older features. From the considerations above, it is not likely that Lorentz factors are the same for all components.

2) The component Lorentz factors are constant, but not equal. The difficulty with this scheme is that if differences between the component Lorentz factors are small, then the situation resembles that of the previous scheme. On the other hand, if the component Lorentz factors differ significantly, then it can result in the chaotic appearance the jet will have in the source rest frame. If we adopt the lowest Lorentz factors from Table 3.2, C3, C3a, C4, and C7 would be found at *larger* distances from the core than C2, in the rest frame of the source. This situation is illustrated in Figure 3.21.

3) The component Lorentz factors vary in time. In this situation, the increase of apparent velocity is caused not only by changing viewing angle, but also by *intrinsic* changes of the component velocity. It can be either the increasing bulk Lorentz factor, or the Lorentz factor of the shock. In view of the arguments against a constant Lorentz factor, we may therefore conclude that the jet components can increase their

rest frame velocity. This implies that acceleration processes are not restricted to the immediate vicinity of the core, but are also present on larger scales in the jet. A detailed description of the component velocity evolution is model dependent. To avoid introducing additional parameters in our consideration, we propose to use the condition of minimal jet kinetic power to derive a plausible shape of the velocity changes. The minimum kinetic power condition is described by Equation 3.12, which becomes an equality in this case. The corresponding evolution of the component kinematics is shown in Figure 3.22. We can see that in this case, the component appearance in the jet rest frame is strictly orderly. The changes of γ required for reproducing such an orderly evolution may seem overly complicated, and difficult to describe by more physical models. However, the dependences in Figure 3.22 suggest clearly that non-linear variations of the component speed are required for satisfactory explanation of the observed component kinematics.

Minimum kinematically allowed Lorentz factor

The actual value of Lorentz factor of the jet plasma is generally unknown, although it can be estimated roughly from X-ray (ZCU95, Unwin *et al.* 1994) or γ–ray flux of an AGN. However, such estimates are usually possible for only a limited number of epochs for which X-ray measurements are available (3C 345 does not seem to have a detectable γ–ray flux; Fichtel *et al.* 1994). As we have shown in the previous section, the component Lorentz factors are likely to vary in the jet rest frame. To incorporate these variations in our subsequent analysis, we need to make an assumption about some plausible type of evolution of the Lorentz factor. We suggest to use, for this purpose, the condition (3.12) for the minimum kinematically allowed Lorentz factor. In the absence of measured values, the γ_{min} condition can provide useful limits for various physical parameters of the jet. Physically, this condition describes the least kinetic power that a jet component with the observed evolution of apparent velocity $\beta_{app}(t)$ can have. This condition will be used for the calculations of component luminosities (Chapter 5, Section 5.3.3), and for the analysis of spectral evolution of C4 and C5 (Chapter 6, Section 6.3.7).

Proper motion

From the component trajectories described in Section 3.2.2, we calculate the proper motion and apparent distance travelled by the components, using equations (3.4), (3.5). Figure 3.23 shows the component proper motions as a function of the travelled distance.

At the latest stages of component life time, the derived proper motion depends on the travelled distance almost linearly. For the oldest component, C1, the proper motion becomes smaller with increasing travelled distance. Although this is consistent with the decreasing flux of C1 at 5 GHz, the component trajectory is poorly known, and it may affect the dependence in Figure 3.23 significantly.

Another component with monotonically decreasing proper motion is C6. A possible explanation for this is that C6 has only been observed very close to the core, where a decrease of proper motion is likely to be found (for instance, in case of a helical geometry of the jet). At comparable separations, the proper motions of C3, C3a, C4, and C7 are also decreasing (see Figure 3.24). The only component that does not show a proper motion decrease is C5. It may be a consequence of a peculiar trajectory of the component (see Figure 3.12). We will discuss this peculiarity in Chapter 6.

The observed consistency of the proper motion behavior suggests that the jet is stable, and the succeeding components have trajectories similar to those of the preceding components. However, there is evidence, in Figure 3.23, for global evolution of the jet. Apart from the two weakest features of the jet (C5 and C6), the proper motion of younger components tends to be higher than that of the older features at the same distance from the core. That is, the succeeding components tend to have stronger acceleration, and achieve the same level of proper motion at shorter distances travelled along the jet. The differences between the slopes are correlated with the estimated epochs of the component origin (see Table 3.1). The proper motions of C1 and C2 vary very weakly with distance. C3, C3a, and C4 have very similar slopes, and close origin epochs. Correlation between the component slopes of proper motion and origin epochs is presented in Figure 3.25. The components slopes $\Delta\mu/\Delta\Theta$ show a steady increase, following the order of component succession. This can be evidence for global changes occuring in the jet. The nature of these changes is unclear. Possible explanations include intrinsic strengthening of the source, changes of physical conditions of the ambient media, and jet precession.

Of these three possibilities, the precession is probably the most likely, since it does not require variations of physical parameters of the jet and central engine. In a precessing jet, the viewing angle can change so that a successive component has more favorable geometry resulting in faster apparent motion.

Relations between C3, C3a, C4, and C5

From the discussion above, we can suggest that C3, C3a, and C4 are closely related in their kinematic properties, and may have been produced by a single outburst, or a series of outbursts occured during the period of violent activity in 3C345 (1976-1980). Component C5 which has its epoch of origin very close to that of C4 can also be included in this group. In Chapter 6 we will attempt to explain the peculiarities of trajectory and proper motion evolution exhibited by C5, with respect to its possible relations with C4. Overall, the four abovementioned components were ejected within four years. For comparison, the preceding C2 and succeeding C6, C7 are separated by 7–8 years from the C3–C5 group.

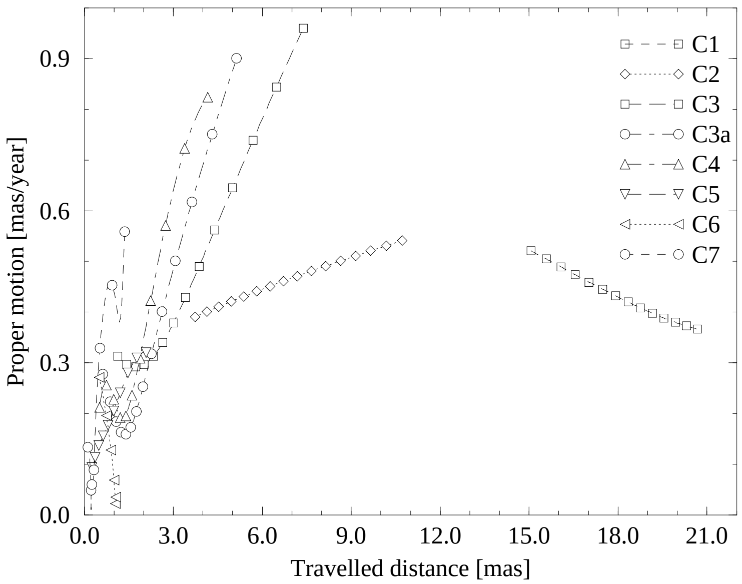

Figure 3.23: Correlation between the component proper motions and distances travelled along the jet.

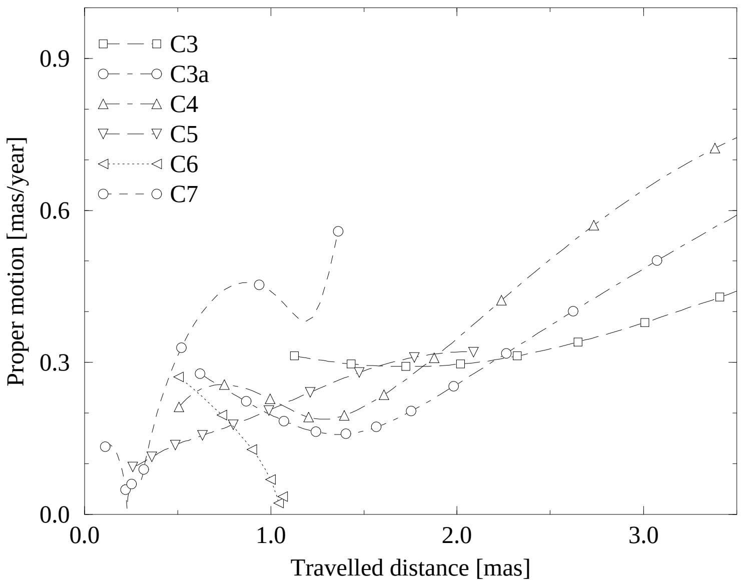

Figure 3.24: Correlation between the component proper motions and distances travelled along the jet: immediate vicinity of the core.

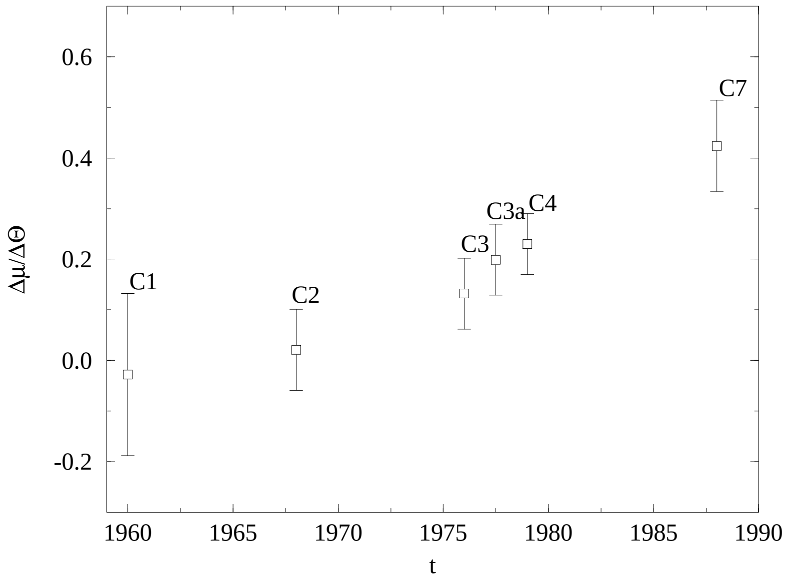

Figure 3.25: Correlation between the slopes of of the component tracks in "proper motion vs. travelled distance" diagram and the component epoch of origin.

3.4 Summary

The main results from the study of the jet kinematics in 3C345 are as follows:

1) Long–term kinematic changes have been studied in the jet components. The component two–dimensional trajectories are reconstructed from the polynomial fits to the component coordinate offsets from the core position.

2) The component two–dimensional trajectories follow similar, overlapping tracks, and outline a continuous picture of a curved jet for distances of up to 20 mas (about $80(h\ \sin_j^{\theta})^{-1}$ pc). The separation of 20 mas from the core can mark a transition point from compact jet to large–scale jet. At this separation the jet finally turns to the direction $\phi \approx -40^{\circ}$ observed in the large–scale jet of 3C345.

3) Three kinematic schemes have been considered to reconstruct the three–dimensional trajectories of the jet components. We have shown that the small–angle solution provides the most realistic account of the jet three-dimensional geometry.

4) Model–imposed kinematic limits for the non-accelerating jet are discussed. We have shown that Lorentz factors are not likely to be same in different jet components. Lorentz factors of individual components must change during the component evolution in order to account for the observed apparent velocities. The change of Lorentz factors implies intrinsic changes of the jet component velocities, and suggests that a mechanism for reacceleration should exist in the jet.

5) The jet components can be separated into three groups, on the basis of their kinematic properties and epochs of origin: the outer jet (C1, C2); the intermediate

jet (C3, C3a, C4, C5); and the inner jet (C6, C7).

6) The proper motions of the inner and intermediate jet components exhibit similar behavior, with increasing distance travelled by the components along the jet. The proper motions of C3, C3a, C4, C6, and C7 decrease within the 1–3 mas distance travelled by the components along the jet. The peculiarity of the trajectory and proper motion of C5 needs to be considered together with its flux, luminosity and spectral properties, in order to make a conclusion about the nature of this component.

7) Changes of the component proper motions may indicate the existence of global kinematic evolution of the jet. The component acceleration is found to be increasing in the younger components. The observed trend can be explained by intrinsic changes of the source, or by the jet precession providing more favorable geometrical conditions for the succeeding components compared to the preceeding jet features. The second explanations appears to be more acceptable.